Article

Low-Altitude Sensing Model: Analysis Leveraging ISAC in Real-World Environments

Xiao Li [1,2,*], Xue Ding [1], Weiliang Xie [1], Wenbo Wang [2], Jinyang Yu [1] and Wen-Yu Dong [2]

1   Mobile and Terminal Technology Research Department, China Telecom Research Institute,
     Beijing 102209, China
2   School of Information and Communication Engineering, Beijing University of Posts and Telecommunications,
     Beijing 100876, China
*   Correspondence: lixiao6@chinatelecom.cn

Abstract: With the explosive growth of unmanned aerial vehicle (UAV) applications in numerous fields, low-altitude networks face formidable challenges in monitoring. In this context, integrated sensing and communication (ISAC) networks through three-dimensional (3D) wide-area sensing have emerged as the key solution. However, the differences in networking mechanisms between communication and sensing, along with the transition from two-dimensional (2D) to 3D networking, complicate the realization of seamless 3D sensing. We aimed to address these challenges by analyzing the sensing capabilities of a single base station and the disparities between communication and sensing. Based on this, an innovative 3D sensing model for ISAC single base stations was proposed, defining the sensing boundaries and providing a foundation for designing the key parameters of ISAC base stations. Additionally, a multi-base station (multi-BS) low-altitude networked 3D sensing cellular-like architecture was proposed, overcoming the limitations of traditional 2D networks and achieving seamless 3D sensing. To validate the effectiveness of the model, comprehensive tests were conducted in both controlled laboratory conditions and real-world commercial network environments. The results show that the model successfully achieved stable and continuous sensing with the expected coverage and accuracy in networked environments.

Keywords: low-altitude networked sensing; integrated sensing and communication; single base station sensing model; cellular-like architecture; unmanned aerial vehicle

1. Introduction

With the rapid development of technologies, the application of unmanned aerial vehicles (UAVs) in the low-altitude domain has become increasingly widespread, particularly in sectors such as transportation, logistics, and public utilities, where they show immense potential [1–3]. It is projected that by 2030, the global drone market will reach a scale ranging from $100 billion to $140 billion [4]. In this context, ensuring low-altitude flight safety and enabling effective UAV regulation have become critically important. The fusion of communication and sensing technologies for low-altitude networked sensing has emerged as the core solution to these challenges. It plays a significant role in building a safe and efficient low-altitude operational environment [5].

The integrated sensing and communication (ISAC) technology offers distinct advantages over traditional sensing methods. As one of the new native capabilities in next-generation wireless networks, ISAC allows for active environmental sensing while simultaneously supporting data transmission. Compared to traditional radar systems, ISAC base

stations offer significant advantages in terms of cost, data transmission, coverage, and resource reuse. A major benefit of wireless sensing over radar is the ability to achieve contiguous coverage through large-scale networking.

Although the ISAC technology provides a fresh perspective for low-altitude sensing, achieving wide-area sensing based on this technology still faces significant challenges [6–10]. A key challenge lies in the inherent differences in coverage characteristics between communication and sensing. Communication signals typically meet coverage needs through single-hop transmission, while sensing signals require reflection from targets, resulting in a multi-hop propagation process. This creates clear differences in coverage range and characteristics, making it difficult to achieve coordinated and ideal coverage during network deployment. Additionally, transitioning from traditional two-dimensional (2D) communication cellular networks to low-altitude three-dimensional (3D) sensing networks presents significant difficulties. The current 5G networks primarily focus on ground communication coverage, while low-altitude coverage and sensing capabilities have not been considered. The traditional hexagonal 2D cellular network model is not suitable for low-altitude environments. Base stations are limited by antenna performance, which prevents them from covering their own tower-top areas. Furthermore, low-altitude signal propagation is primarily line-of-sight (LOS), which is different from the non-line-of-sight (NLOS) propagation commonly found in urban areas. These differences render traditional network models unsuitable for low-altitude applications. Meanwhile, the low-altitude ISAC environment is complex and subject to various interferences, such as other communication devices and the impact of terrain, further complicating the construction of stable and efficient low-altitude networked sensing systems. Overcoming these challenges and building a network that meets the low-altitude "wide-area, seamless, 3D" sensing requirements has become an urgent and critical issue.

This paper adopts Work Mode 1, as mentioned in IMT-2020, specifically, the single base station responsible for both the transmission and reception nodes [11,12]. This approach was chosen due to its significant advantages. In Work Mode 1, base stations have independent sensing capabilities and do not rely on other base stations to complete sensing tasks. This eliminates the sensing errors caused by the asynchronous operation of the transmission and reception nodes, significantly improving sensing accuracy. In the complex low-altitude environment, this independent operational feature reduces reliance on other nodes, thus minimizing the risk of sensing failure due to network node faults or synchronization issues. Furthermore, this mode is relatively easy to implement, requiring no complex protocol interactions or coordination mechanisms between nodes. It is also easier to upgrade and deploy on the existing base station equipment, effectively reducing system complexity and costs, and providing a more reliable and feasible technical foundation for the construction of low-altitude networked sensing models.

1.1. Background

Although progress has been made in the low-altitude ISAC networks, there are still many shortcomings. Current research mainly focuses on signal processing, algorithm optimization, network models, coverage models, and simulation verification. However, these studies often lack depth in model design or capability integration, or they have limitations in practical validation, failing to fully meet the requirements for accurate coverage, capability fusion, and real-world application in low-altitude ISAC networks.

To address the challenge of seamless low-altitude sensing coverage in cellular networks, studies [6,13] have focused on beamforming optimization for dual-base ISAC systems and multi-static systems with coordinated multi-point joint transmission (CoMP-JT), all using successive convex approximation (SCA) algorithms. However, these studies

focus on signal processing and algorithm optimization and do not deeply explore network coverage model design. As a result, the sensing boundaries and coverage of a single base station in low-altitude scenarios remain unclear. Lei et al. [14] proposed a radar sensing coverage model that comprehensively considers indicators such as range, field of view, and resolution. However, it only focuses on the radar independently and does not consider the integration of communication and sensing, making it difficult to support the complete coverage theory of low-altitude ISAC networks. Li et al. and Wang et al. [6,15] discussed the sensing coverage range and the general model in communication-sensing networks. However, their research focused on ground networks, and the feasibility and reliability of the model in low-altitude environments are questionable. In response to the abovementioned issues, our paper, through in-depth analysis of the vertical field of view (FOV) of base station antennas and the differences in cell radius and beam characteristics between communication and sensing, constructs a 3D sensing model for a single ISAC base station. This model accurately defines the sensing boundaries and range, provides a theoretical basis for the sensing capabilities of low-altitude networks, and fills the gap in the design of the key parameters for communication-sensing fusion.

Zhao et al. [16] proposed a multi-base station (multi-BS) collaborative networking mode for UAV scenarios, but the content is insufficiently detailed, lacks specific modeling methods, and is unable to address the coverage issue at base station tower tops. Wang et al. [17] designed a multi-BS integrated sensing and communication system for 6G macro–micro collaboration. Still, its coverage range calculation method is primarily targeted at ground networks and does not account for the specific characteristics of low-altitude environments. Several studies [18–26] analyzed low-altitude coverage issues from the communication perspective, such as by analyzing the impact of base station height, UAV altitude, and other parameters on coverage and validating the channel model through testing [18,19]; by proposing 3D communication system models and new cellular structures [20,21]; by improving cellular sector partitioning and 3D networking schemes [21–24]; and by validating the feasibility of 5G low-altitude communication coverage [25,26]. However, these studies do not consider the fusion of sensing capabilities, and their network solutions have low feasibility for large-scale commercialization. To address the coverage issue at base station tower tops, our paper proposes a multi-BS complementary coverage method and designs a 3D sensing-based cellular-like topology for low-altitude multi-BS networking, overcoming the limitations of traditional 2D network models.

On the other hand, the existing research on the practical validation of ISAC fusion networks shows clear gaps, with most studies lacking real-world testing, leading to a disconnect between theory and actual application. Many models remain at the theoretical stage without real-world validation, making it difficult to achieve the expected results in complex environments. Specifically, the ISAC coverage models proposed in [6,15] lack real-world testing and cannot guarantee their applicability in low-altitude scenarios. While [19] validated communication channel models through testing, the focus was solely on communication coverage, without addressing the validation of sensing capabilities. This study proposed an innovative experimental strategy, conducting single base station sensing capability tests in a millimeter-wave (mmW) frequency far-field over-the-air (OTA) anechoic chamber, with precise parameter control to validate the single base station model. Additionally, leveraging the world's first commercial mmW ISAC network, we collaborated with leading industry suppliers to set up an outdoor testing platform to verify the effectiveness of the sensing network topology in real-world scenarios. This approach fills the gap in the practical validation of ISAC fusion networks, providing technical support for low-altitude ISAC base station network construction and opening new paths for future research and engineering practices.

1.2. Contributions

Based on the current research, the existing network models in the low-altitude ISAC field show significant limitations in achieving "wide-area, seamless, and 3D" low-altitude network sensing based on the ISAC technology. The lack of theoretical network models has seriously hindered the practical deployment of ISAC networks. While a few studies on low-altitude coverage rely on simulations, they lack real-world testing and have not performed in-depth analysis from a holistic view of ISAC low-altitude networks. Therefore, this paper proposes an innovative low-altitude wide-area sensing model based on ISAC base stations, aiming to fill this critical gap. By overcoming the shortage of traditional 2D network models, this paper introduces a seamless coverage solution in 3D space, optimizing base station layout and functionality to address the differences between the communication and sensing requirements, thereby building a low-altitude network model with enhanced sensing capabilities that improve sensing efficiency and reliability in low-altitude environments.

The results of this study not only provide theoretical support for the development of low-altitude networks, but also serve as a reference for other mobile network operators or countries, especially considering the expected continuous growth of the low-altitude economy in the coming years. Moreover, the proposed method is general and can be applied to 6G networks in the future. The main contributions of this paper are as follows:

- This paper constructs a 3D sensing model for a single ISAC base station operating in a single base station responsible for both the transmission and reception nodes. It analyzes the influence on vertical FOV of base station antennas, and the differences in cell radius and beam characteristics between communication and sensing. Compared to previous studies, this model more precisely defines the sensing boundaries and range of a single base station, providing a more accurate theoretical basis for low-altitude network sensing capabilities. This achievement not only contributes to a deeper understanding of the basic characteristics of low-altitude ISAC networks, but also offers innovative ideas for designing the key parameters of ISAC fusion base stations, laying a theoretical foundation for the development of low-altitude ISAC networks.

- To address the issue of base station tower top blind spots, this paper proposes a multi-BS complementary coverage method and designs a 3D sensing-based cellular-like topology for low-altitude multi-BS networking. Compared to traditional 2D network models, this topology overcomes the limitations in low-altitude 3D coverage. By optimizing base station layout and signal coverage, it achieves seamless 3D sensing in low-altitude environments, significantly improving the accuracy and reliability of wide-area low-altitude sensing. This innovative design provides a practical solution for the real-world application of low-altitude ISAC networks and lays the foundation for the widespread adoption of low-altitude sensing technology across various fields.

- To validate the feasibility of the single base station model under ideal conditions, this paper conducts the first laboratory tests on the sensing boundary of a single base station in an mmW frequency far-field OTA anechoic chamber. Additionally, based on the world's first commercial mmW ISAC network, a real-world testing platform is set up in collaboration with leading equipment suppliers for outdoor field testing, successfully validating the effectiveness of the sensing network topology in actual scenarios. This combination of laboratory and real-world commercial network testing provides a comprehensive and reliable reference for the network deployment of low-altitude ISAC base stations, filling the gap in practical testing and verification in this field and providing crucial technical support and practical experience for future research and engineering practices.

The remainder of this paper is structured as follows. Section 2 delves into the 3D sensing model for the single base station responsible for both transmission and reception

in the ISAC network, elaborating on its key components and operational principles. In Section 3, a cellular-like topological structure for 3D sensing in a multi-BS low-altitude networking scenario is proposed, highlighting its innovative features and advantages in the low-altitude environment. Section 4 showcases several experimental results and an in-depth analysis of the models, validating the effectiveness and performance improvements of the proposed models. Finally, Section 5 summarizes the research, drawing conclusions and pointing out potential directions for future work.

2. The Model of Single Base Station 3D Sensing

In this section, we delve into the single base station sensing capabilities within low-altitude sensing networks, clarify their distinctions from traditional base stations and propose targeted models and key parameter design schemes.

2.1. Analysis of Single Base Station Sensing Capabilities

Single base station sensing is fundamental to achieving seamless 3D networked sensing in a low-altitude ISAC network. At a certain altitude, the coverage area of single base station sensing resembles a sector. Hardware capabilities of a single ISAC base station are mainly constrained by factors such as the horizontal and vertical FOVs of the base station antenna, as well as the coverage height and tilt angle of the active antenna unit (AAU). The farthest sensing boundary is determined jointly by signal propagation characteristics, system gain and loss, and environmental factors. Based on these factors, we can determine the sensing boundaries in various directions by calculating the sensing signal-to-noise ratio (SNR) and ensuring it is not below the minimum sensing threshold. This can ultimately meet the requirements for 3D continuous coverage networking of station spacing. The key parameters in the radar equation include signal transmission power, transmission and reception antenna gains, carrier wavelength, the radar cross-section (RCS) of the target, and the distance between the target and the radar, among others [27]. A mathematical model for the sensing SNR based on the radar equation has been established to quantify the performance of single base station sensing coverage. The SNR of the sensing target can be expressed as follows:

$$\text{SNR} = \frac{\sigma P_t G_r G_t \lambda^2 n \tau}{(4\pi)^3 R^4 L N_0}, \tag{1}$$

where σ represents the RCS of the target, P_t denotes the transmission power, G_r and G_t are the reception and transmission antenna gains, respectively, λ is the carrier wavelength, n and τ are the total cumulative number of signals and transmission duration (related to the sensing frame structure design), R is the distance between the target and the base station, L is the RV processing loss, and N_0 represents the noise, including interference.

The antenna gains G_r and G_t are closely related to the angle of the sensing target relative to the base station antenna and can be expressed as follows:

$$G(\theta) = G_{\max} \cdot \cos^n(\theta), \tag{2}$$

where $G_{\max}$ is the maximum antenna gain, n is the antenna gain attenuation coefficient, and θ is the angle between the target and the antenna's normal direction. The greater the deviation from the central angle, the lower the antenna gain. Therefore, the coverage performance at the edge of the sensing area is usually lower than that in the central area.

The introduction of sensing functionality brings interference issues among sensing operations, as well as between sensing and communication. Moreover, the sensing signals transmitted into the air inevitably cause remote interference. Therefore, under the networking conditions, for N_0, it is necessary to take into account the adjacent station's sensing in-

terference $P_{\text{neighbor-sensing}}$, the uplink communication user interference $P_{\text{uplink-communication}}$, and the remote interference $P_{\text{remote-interference}}$ on the basis of the background noise P_{noise}. Therefore, we can obtain the following:

$$N_0 = P_{\text{noise}} + P_{\text{neighbor-sensing}} + P_{\text{uplink-communication}} + P_{\text{remote-interference}} \tag{3}$$

The neighboring station's sensing interference power $P_{\text{neighbor-sensing}}$ can be expressed as follows:

$$P_{\text{neighbor-sensing}} = \sum_{k=1}^{N} \left(\frac{\sigma_{\text{n}}(k) P_{\text{nt}}(k) G_{\text{nr}}(k) G_{\text{nt}}(k) \lambda^2 n\tau}{(4\pi)^3 R_{\text{n}}^4(k)} \gamma(k) \right), \tag{4}$$

where N is the total number of neighboring stations, $\sigma_{\text{n}}(k)$ is the RCS of the target at the kth neighboring station, $P_{\text{nt}}(k)$ is the transmit power of the kth neighboring station, $G_{\text{nr}}(k)$ and $G_{\text{nt}}(k)$ are the reception and transmission antenna gains of the kth neighboring station, respectively, and $R_{\text{n}}(k)$ is the distance between the sensing target and the kth neighboring station; $\gamma(k)$ is the signal attenuation coefficient of the sensing signal from the kth neighboring station affected by multipath effects, typically ranging between 0 and 1.

The uplink communication interference $P_{\text{uplink-communication}}$ can be expressed as the sum of the power of N uplink users within the sensing bandwidth B:

$$P_{\text{uplink-communication}} = \int_{-B/2}^{B/2} \left(\sum_{k=1}^{N} (P_{\text{u}}(k, b)) \right) \tag{5}$$

Furthermore, in dense urban scenarios (Urban Macro), $P_{\text{remote-interference}}$ can be further extended based on the path loss model for macro base station UAVs (RMa-AV). The RMa-AV model is derived from the RMa model [28], and $P_{\text{remote-interference}}$ can be expressed as follows:

$$P_{\text{remote-interference}} = \int_{-B/2}^{B/2} \left(\sum_{k=1}^{N} \left(\begin{array}{c} 10 \max\left(3.7 - 0.8\log_{10}(h_{\text{UT}}), 2\right) \log_{10}(d_{\text{3D}}(k)) \\ -35.5 + 18.5\log_{10}(h_{\text{UT}}) + 20\log_{10}\left(\frac{40\pi f_{\text{c}}(k)}{3}\right) \end{array} \right) \right), \tag{6}$$

where h_{UT} is the target flight altitude, $d_{\text{3D}}(k)$ is the radial distance between the target and the kth remote base station, and $f_{\text{c}}(\text{k})$ is the center frequency of the kth remote base station.

Given the minimum sensing threshold S_{min}, the maximum sensing distance R_{max} for a single station can be expressed as follows:

$$R_{\text{max}} = \left[\frac{\sigma P_{\text{t}} G_{\text{t}} G_{\text{r}} \lambda^2 n\tau}{(4\pi)^3 L N_0 S_{\text{min}}} \right]^{\frac{1}{4}}. \tag{7}$$

It can be seen that station spacing is positively correlated with the maximum sensing distance of a single station. Meanwhile, the maximum sensing distance of a single station is positively correlated with parameters such as transmit power, antenna gain, target RCS, and gain accumulation, and negatively correlated with noise and SNR threshold.

2.2. Differentiation Analysis

Traditional base stations and low-altitude ISAC base stations clearly exhibit significant differences in design objectives, network coverage, and service requirements. Traditional base stations typically aim for comprehensive coverage of ground communication networks. They primarily serve large-scale mobile users and focus on providing stable communication signals. Traditional base stations typically calculate coverage radius and evaluate station spacing based on edge rate and reference signal receiving power (RSRP) metrics. In contrast,

low-altitude ISAC base stations emphasize the precise identification and sensing of aerial targets, mainly playing a crucial role in detecting airborne objects, such as UAVs. Unlike traditional base stations, the low-altitude ISAC base station must further consider the sensing performance in addition to the communication coverage, especially in eliminating sensing blind spots and ensuring target sensing accuracy.

The spacing between ground base stations in traditional cellular networks is generally about 1.5 times the cell coverage radius, enabling seamless 2D planar coverage through cellular networking. In contrast, in low-altitude 3D sensing networks, due to the limitations mentioned above imposed by the vertical FOV of antennas, sensing blind spots exist in the tower-top area. To meet low-altitude sensing requirements, the proportional relationship between station spacing and cell radius must be adjusted to ensure that the coverage between base stations eliminates blind spots and enhances sensing capabilities.

The goal of communication services is data transmission, and both main lobe and side lobe coverage can meet the requirements as long as the communication SNR reaches the demodulation threshold of the receiver. However, for sensing modes, especially the accurate detection of target positions, reliance is typically placed on the echoes of the main lobe signals. In contrast, interference from side lobe signals must be suppressed. Therefore, sensing services impose higher demands on coverage areas. In low-altitude ISAC networks, to eliminate sensing blind spots and ensure target detection accuracy, the design of the cell radius often requires smaller station spacing compared to traditional communication networks, emphasizing signal strength and interference suppression capabilities.

2.3. Model and Key Parameters Design

As illustrated in Figure 1, in low-altitude 3D ISAC networks, sensing range is constrained by the vertical FOV of the antenna, limiting the scanning range to a specific angular extent. This limitation results in coverage blind spots in the tower-top area of the base station.
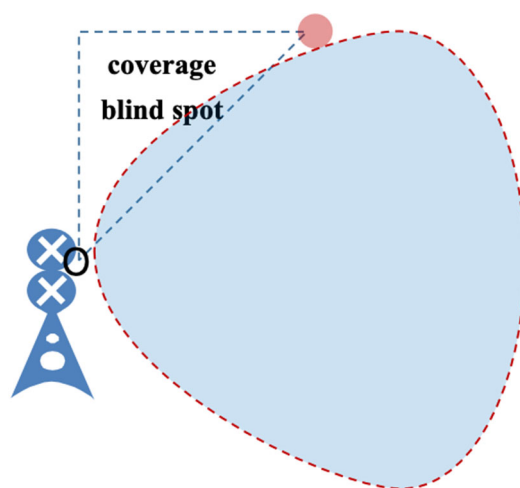

Figure 1. Vertical FOV of an antenna.

The coverage capability of base stations varies at different altitudes. As the altitude increases, the horizontal coverage range decreases. The area of the coverage blind spots at the tower top expands, as shown in Figure 2. O represents the antenna coordinate point, A represents the farthest sensing boundary point in the direction at the same height as the antenna, and OA denotes the radial distance between point O and point A. The key to achieving continuous 3D coverage at low altitudes lies in ensuring seamless primary lobe coverage at the maximum altitude, which imposes specific requirements on the vertical FOV α of the base station antenna.
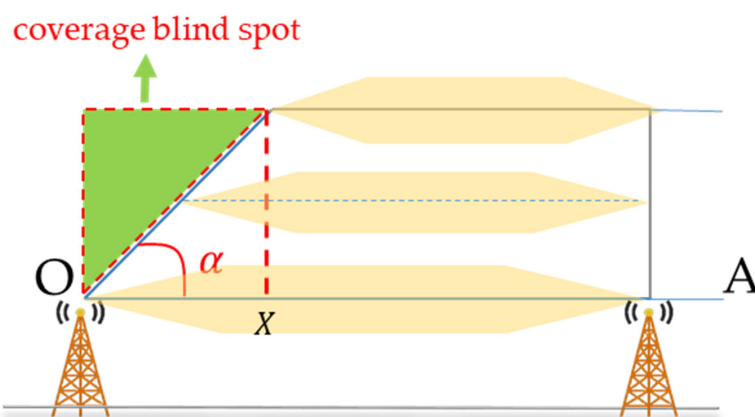
Figure 2. Low-altitude network coverage at different altitudes.

We constructed a hexagonal cellular-like network topology to achieve effective coverage in the low-altitude area. In low-altitude sensing scenarios, ensuring continuous primary lobe coverage at the maximum altitude is crucial, which requires maximizing the coverage range of the main lobe of the local base station while minimizing the coverage of the main lobe of neighboring stations over the blind spots at the tower top of the local base station. By precisely balancing the coverage ratio between the main lobe of the local station and those of neighboring stations, we could achieve continuous coverage across different altitudes.

In the low-altitude network topology at the highest defined altitude, as shown in Figure 3a, it is clear that the main lobes of neighboring stations cover the tower-top area of the local base station. However, when focusing on lower altitudes, the situation changes. As the coverage range of the base station increases at lower altitudes, overlapping coverage becomes evident, particularly at the horizontal height of the antenna, as intuitively depicted in Figure 3b.
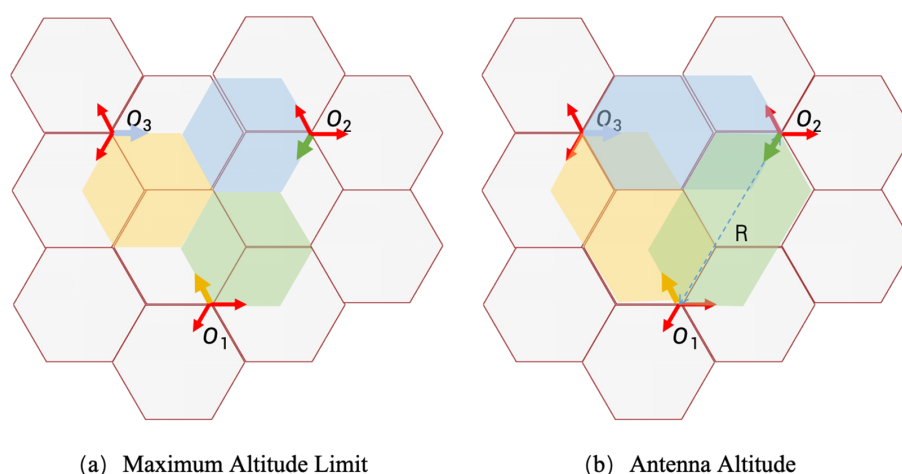

(a) Maximum Altitude Limit   (b) Antenna Altitude

Figure 3. Low-altitude neighboring cell coverage over the tower top.

Based on the above analysis, we further proposed an integrated low-altitude sensing model, as illustrated in Figure 4. The definitions of O and A remain consistent with those in Figure 1. Point C is the intersection point between the direction of the maximum vertical FOV extension of the antenna and the maximum flight altitude. OC is the radial distance between point O and point C. Point B is the maximum flight altitude point of A, extending vertically upwards. Point X is the intersection of the vertical line from C downward with the OA, and the radial distance from point O to point X is denoted as s. Using B and C as the longest diagonals, we constructed a horizontal regular hexagon CDEBGF. At the maximum flight altitude, the main lobe coverage area of one sector of the BS0 base station

is the area enclosed by CDEBGF. Q and N are the vertical projections from points E and G to the plane at the antenna height, while OM and OP are parallel and equal in length to AQ and AN, respectively. Thus, on the antenna height plane, a hexagon OPQANM is formed, representing the main lobe coverage area of one sector of BS0 at the base station height level. Additionally, H is the vertical projection from point O to the maximum flight altitude, h_1 represents the distance OH, and d represents the distance OA, which is the station spacing. The angle between OP and OA is the horizontal FOV γ of the antenna. Under typical three-sector cellular networking conditions, γ is usually set to 60°.
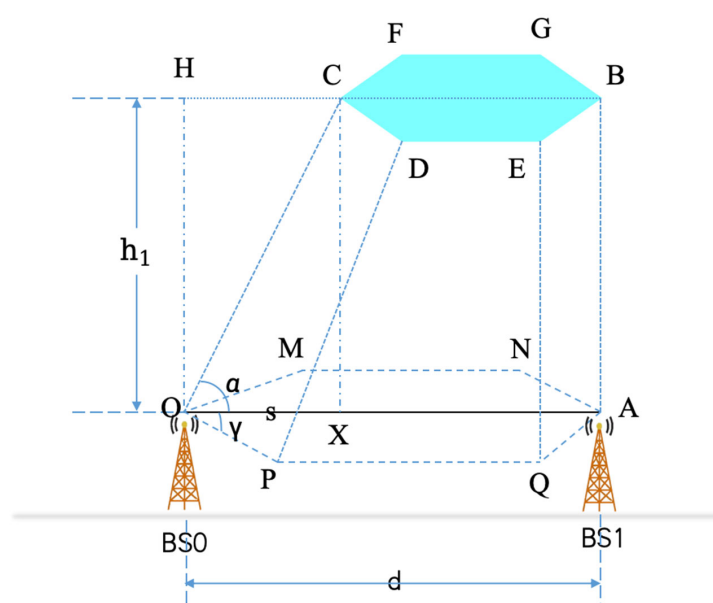

Figure 4. Single base station sensing 3D model.

To construct an accurate mathematical model for analyzing the coverage characteristics of base stations in low-altitude sensing networks, we defined the location of the base station antenna as the coordinate origin $O(0,0,0)$. The direction of the line segment OA was defined as the positive direction of the X-axis, and the direction of the line segment OH was defined as the positive direction of the Y-axis, with points D and E both located in the first quadrant. Based on this, a 3D Cartesian coordinate system was established. Through derivation and calculation, the precise coordinates of each point were determined as follows:

$$\begin{cases} A(d,\ 0,\ 0) \\ B(d,\ h_1,\ 0) \\ C(s,\ h_1,\ 0) \\ D\left(\frac{d+3s}{4},\ h_1,\ \frac{\sqrt{3}(d-s)}{4}\right) \\ E\left(\frac{3d+s}{4},\ h_1,\ \frac{\sqrt{3}(d-s)}{4}\right) \\ F\left(\frac{d+3s}{4},\ h_1,\ -\frac{\sqrt{3}(d-s)}{4}\right) \\ G\left(\frac{3d+s}{4},\ h_1,\ -\frac{\sqrt{3}(d-s)}{4}\right), \\ M\left(\frac{s}{2},\ 0,\ -\frac{\sqrt{3}s}{2}\right) \\ N\left(\frac{3d+s}{4},\ 0,\ -\frac{\sqrt{3}(d-s)}{4}\right) \\ P\left(\frac{s}{2},\ 0,\ \frac{\sqrt{3}s}{2}\right) \\ Q\left(\frac{3d+s}{4},\ 0,\ \frac{\sqrt{3}(d-s)}{4}\right) \\ H(0,\ h_1,\ 0) \end{cases} \qquad (8)$$

Since HB = OA = d and HC = OX = s, the relationship between the vertical FOV α of the base station towards the air, the maximum vertical coverage height h_1, and the coverage blind spots can be expressed as follows:

$$\alpha = \arctan\frac{h_1}{s},\tag{9}$$

The horizontal distance ratio of the neighboring station's coverage over the top of the local station tower (HC/OA) can be expressed as follows:

$$\omega = \frac{h_1}{d\cdot\tan\alpha}\times100\%,\tag{10}$$

which also represents the relationship between the maximum coverage blind spots and the inter-station distance. It further clarifies: (1) the coverage capability of single base stations, (2) the performance degradation caused by vertical FOV limitations, and (3) references for subsequent designs where adjacent stations compensate for the tower-top coverage blind spots of local stations.

In summary, it can be concluded that the main lobes of neighboring stations cover the tower top blind spots of the local base station. Specifically, the coverage area of the local base station's main lobe and the neighboring stations' main lobes exhibit a proportional relationship, as expressed in Equation (10). This relationship is jointly determined by three key parameters: the base station coverage height, the vertical FOV of the base station, and the station spacing. These parameters interact and are interrelated, collectively influencing the coverage characteristics and complementary relationships between base stations. Further analysis revealed that when station spacing and coverage height remained constant, a larger vertical FOV of the base station implied a broader coverage range of the local base station, thereby reducing the reliance on neighboring stations for covering the tower-top area. The model emphasizes optimizing antenna design and base station coverage areas, particularly in low-altitude sensing networks. Effective optimization methods are proposed by analyzing the relationships among antenna radiation angles, base station height, FOV, and station spacing. Combined with hexagonal grid planning, the model provides theoretical support for network coverage in low-altitude areas, optimizes base station design, and enhances sensing performance.

3. Multi-BS Networking with Cellular-like Topology

Building on the single base station 3D sensing model in the previous section, this section focuses on multi-BS networking with a cellular-like topology. This approach is crucial for achieving seamless 3D sensing in low-altitude sensing networks.

We extend the traditional cellular communication topology by elongating and translating in the vertical dimension. This allows us to achieve continuous sensing with a cellular-like network at different heights across horizontal cross-sections. The relationship between the station spacing d and the coverage radius R directly affects the sensing continuity and interference in overlapping areas. As analyzed in the previous section, the station spacing should satisfy $d \leq R$ to ensure seamless coverage. When taking $d = R$, for example, the networked sensing 3D structure is shown in Figure 5.

Further, the sensing network conditions at different heights show significant differences, as illustrated in Figure 6. Different colors represent different cells. At the altitude limit, a standard hexagonal cellular topology was adopted to ensure continuous coverage. As the height gradually decreased, the hexagons elongated, and overlapping occurred in the cellular structure. Additionally, the lower the altitude, the more susceptible the sensing network was to the influence of obstacles. Although overlapping areas may lead to

resource loss, de-duplication through multi-BS sensing may help reduce the probability of missed detections.
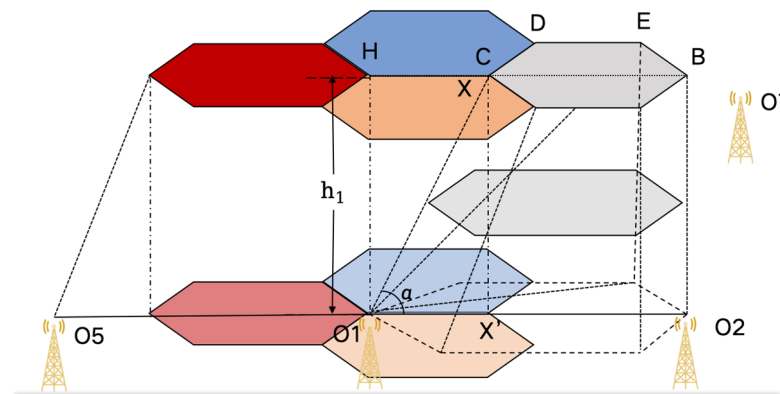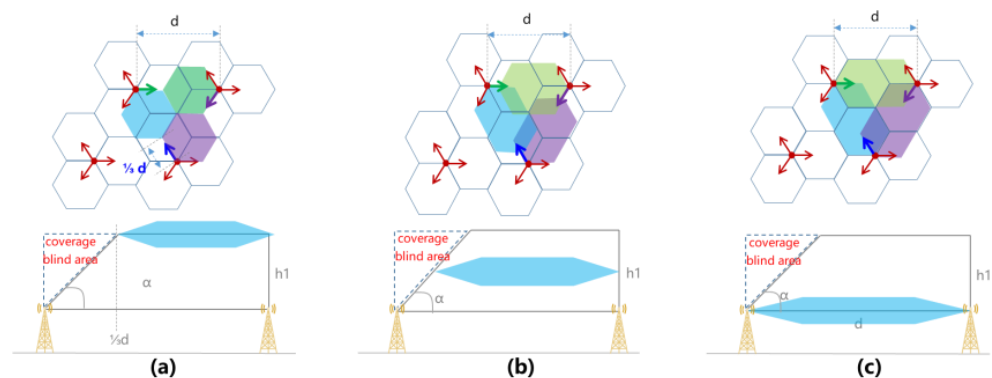

Figure 5. Networked sensing 3D model.

Figure 6. Low-altitude sensing network topology at different altitudes. (**a**) the altitude limit height (**b**) general height floor (**c**) the base station height.

Furthermore, from the perspective of multi-BS networked cellular joint sensing, sensing blind spots are most likely to occur at the altitude limit. As shown in Figure 7, at the maximum coverage height, the tower top blind spot of O_1 was covered by the main lobes of three neighboring sectors, O_3, O_5, and O_7. The same color represents the same base station. Taking the main lobe of the O_1's sector pointing to the lower-left direction, which covered the blue area between O_1 and O_2 as an example, the vertical FOV α of O_1 affected the position of point X. Point X was the outer edge of the tower top blind spot at the maximum height. When the vertical FOV of O_1 was larger, X was closer to O_1; when the vertical FOV was smaller, X was closer to O_2. The position of X affected the coverage requirements of the three neighboring stations for the tower top blind spot of O_1. For example, for neighboring station O_3 covering the O_1's tower top, the antenna's normal direction of the O_3's right-pointing sector was along O_3O_1. When the FOV of O_1 was smaller, the angle between O_3X and the O_3's antenna's normal direction increased. Since the beam gain in the O_3X direction decreased more significantly as the deviation from the O_3 normal direction increased, multi-BS networking needed to consider the coverage capabilities of the main lobe beam. Specifically, it needed to determine whether the main lobe beam of O_3 could cover the area between O_1 and X to compensate for the tower top blind spot of O_1.
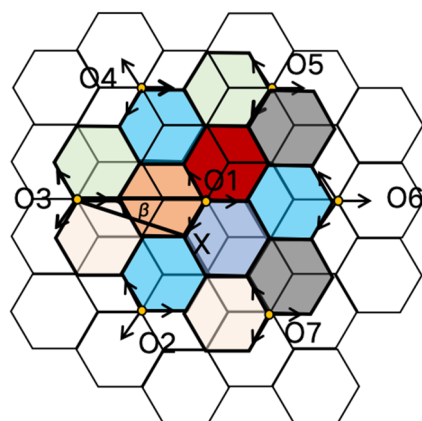
Figure 7. Multi-BS networked blind spot coverage by neighboring stations.

Specifically, under the station spacing *d*, the angle *β* by which O_3X deviates from the antenna's normal direction O_3O_1, can be expressed as follows:

$$\beta = \frac{\gamma}{2} - \arctan \frac{d - \frac{2 \cdot h_1}{\tan \alpha}}{\sqrt{3}d}. \tag{11}$$

In summary, the design of neighboring stations' coverage over the tower top blind spot of the local station needs to consider the vertical FOV of the local station's antenna, the coverage height, the beam gain of the neighboring stations, and the station spacing.

The research findings above provide crucial theoretical foundations for constructing a multi-BS networked cellular-like sensing topology model and designing the key parameters. In the process of building a low-altitude ISAC network, achieving seamless 3D sensing areas is the primary task. Based on the relationship between station spacing *d* and coverage radius *R*, it is necessary to plan the station spacing and the cell radius precisely. The relationship is that $d \leq R$, and when $d = R$, a specific networked sensing 3D structure can be formed. Through such a design, on the one hand, the continuity of the sensing area can be ensured. On the other hand, signal interference in overlapping areas can be effectively reduced, enhancing the overall stability and reliability of sensing.

From the perspective of vertical coverage height, the networking modes at different altitude layers differ significantly. A standard hexagonal cellular topology was adopted at the altitude limit, as this classic structure ensures continuous signal coverage. As the height gradually decreased, the hexagonal structure underwent stretching deformation, leading to overlapping between cells. The increase in overlapping areas reduced the probability of missed signal detection and improved the accuracy of low-altitude sensing. Meanwhile, when designing the antenna FOV of base stations, the influence of the local station's vertical FOV *α* must be fully considered. This parameter directly determines the position of the outer edge of the tower top blind spot at the maximum coverage height. Consequently, it influences the requirements for neighboring stations to cover the local station's tower top blind spot.

When considering the coverage of neighboring stations over the local station's tower top blind spot, the beam gain of neighboring stations is a critical factor that cannot be overlooked. Under the given station spacing *d*, the angle by which the beam deviates from the normal direction must be carefully addressed. Only through precise control of this angle can the sensing capability of neighboring stations meet the requirements, effectively fill the local station's tower top blind spot, minimize sensing blind spots to the greatest extent, and thereby significantly enhance the overall performance of a low-altitude ISAC network.

4. Performance Verification and Analysis

This section focuses on the performance analysis of a low-altitude network sensing model based on ISAC. A series of rigorous tests were conducted thoroughly to evaluate the performance of our model.

This series of tests, from ideal environments to real-world scenarios and from single base station to networked systems, comprehensively verified the performance of the sensing model, providing a solid foundation for the model application and optimization.

4.1. Ideal OTA Test Environment

To verify the capability range of the single base station model under ideal conditions, an OTA anechoic chamber environment was built based on the mmW frequency band for testing. As shown in Figure 8, the AAU was placed on a turntable, allowing it to rotate at a specific angle. The antenna of the target simulator was placed ten meters away from the AAU along the normal direction of the AAU antenna. The baseband unit (BBU) and target simulator were placed outside the anechoic chamber and managed uniformly, with wired connections to the AAU and the antenna of the target simulator. The control center was connected to the BBU, antenna turntable, target simulator, and anechoic chamber for integrated management, synchronizing control time, relative angles, and positions of all test equipment.
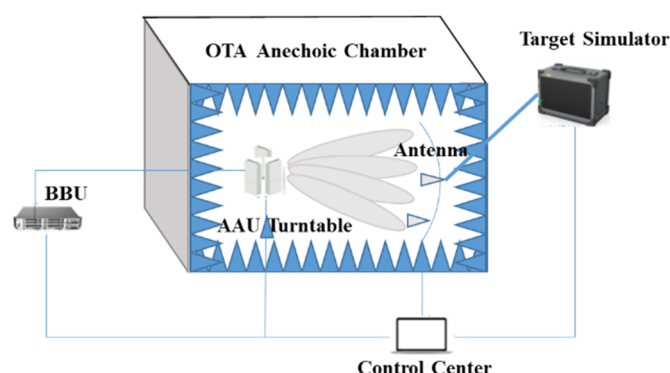

Figure 8. OTA sensing test environment.

The real environment is shown in Figure 9. To accurately present the sensing performance, the minimum size of the anechoic chamber should meet the conditions for a Fraunhofer environment as follows:

$$d_{\text{FF}} \geq \frac{2d_{\text{AAU}}^2}{\lambda} \tag{12}$$

where d_{FF} is the distance from the AAU to the antenna, d_{AAU} is the maximum dimension of the AAU, and λ is the wavelength of the test frequency. All units are in meters. This test was based on the 26 GHz mmW frequency band, and according to calculations, d_{FF} should have been greater than 5.9 m. The actual environment was 10 m.

The turntable used for the test was the HBTE, with the horizontal and vertical angle precision of 0.1°. The radar target simulator WRTE-PRO-1 from RACO simulated the UAV-reflected echo signals. The test base station used a 5G-A mmW ISAC base station from one of the most mainstream equipment vendors. The AAU had a vertical FOV of 40° and a mechanical tilt angle of 0°. The specific single base station 3D sensing model is shown in Figure 10. The sensing waveform combined a continuous wave and a pulse wave.
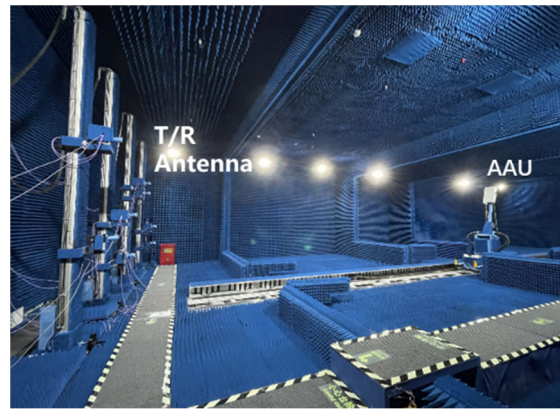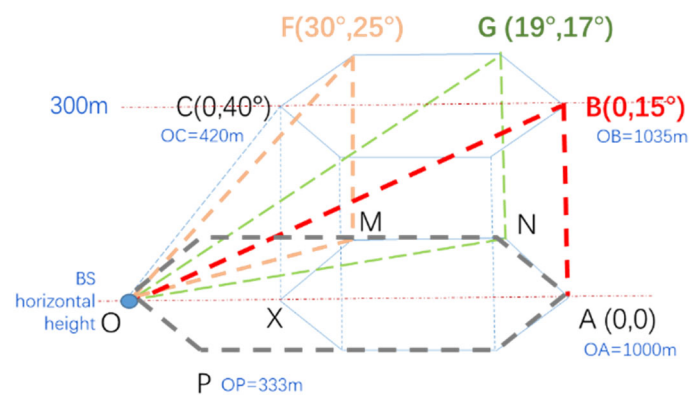
Figure 9. OTA environment.

Figure 10. Single base station 3D sensing model for the OTA test.

The carrier configuration of the AAU is shown in Table 1. The system parameters are shown in Table 2.

Table 1. Carrier configuration.

System	Frequency (GHz)	Bandwidth (MHz)	Band No.	Duplex Mode
5G-A	26	20	n257	TDD

Table 2. System parameters.

Notation	Parameter	System Value
σ	RCS of the target	0.01 m^2
P_t	Transmission power	40 dB
G_r	Reception antenna gains	35 dB
G_t	Transmission antenna gains	35 dB
n	Total cumulative number of signals	64
τ	Total transmission duration of signals	4 μs
L	RV processing loss	4 dB
N	Number of neighboring stations	0

4.2. Single Base Station OTA Test

First, the target was designed to move away from the AAU along the antenna's normal direction (OA direction) at a speed of 1 m/s, starting from the minimum distance supported by the system. The distance R_{min1}^{+} where the target stably appeared and the distance R_{max1}^{+} where the target was stably lost were recorded. Then, the target moved towards the AAU

along the normal direction at a speed of 1 m/s, starting from the maximum supported distance. The distance R_{max1}^- where the target stably appeared and R_{min1}^- where the target was stably lost were recorded. These steps were repeated to obtain R_{min2}^+, R_{max2}^++, R_{max2}^-, and R_{min2}^-. The minimum sensing distance R_{min} and maximum sensing distance R_{max} were then calculated as follows:

$$R_{\text{min}} = \frac{R_{\text{min1}}^+ + R_{\text{min2}}^+ + R_{\text{min1}}^- + R_{\text{min2}}^-}{4} \tag{13}$$

$$R_{\text{max}} = \frac{R_{\text{max1}}^+ + R_{\text{max2}}^+ + R_{\text{max1}}^- + R_{\text{max2}}^-}{4} \tag{14}$$

The base station sensing results are shown in Table 3.

Table 3. OTA sensing distance range test results.

Test Data	Results (m)
R_{min1}^+	0.02
R_{max1}^+	1001.71
R_{min1}^-	0.08
R_{max1}^-	992.42
R_{min2}^+	0.01
R_{max2}^+	1005.56
R_{min2}^-	0.05
R_{max2}^-	1001.20
R_{min}	0.04
R_{max}	1000.22

The average of the nearest point along the OA direction was 0.04 m, and the farthest point was 1000.22 m. This resulted in a discrepancy of 0.02% from the theoretical range, which could be considered in line with the theoretical expectations.

Next, the angle test was conducted at a distance of 300 m along the OA direction from the AAU. The AAU turntable was rotated horizontally until the target was no longer sensed. The current horizontal angle of the turntable was recorded as $\theta_{\text{horizontal}}$. The horizontal angle of the AAU turntable was then restored to the OA direction. The AAU turntable was rotated vertically downwards until the target was no longer sensed, and the current vertical angle of the turntable was recorded as θ_{vertical}. The maximum horizontal and vertical angles were given as shown in Table 4.

Table 4. OTA sensing angle range test results.

Test Data	Recorded Value (°)	Theoretical Value (°)
$\theta_{\text{horizontal}}$	59.95	60
θ_{vertical}	40.28	40

It can be seen that the horizontal angle differed from the theoretical value by only 0.08%, while the vertical angle differed by 0.7%. The main reason for the discrepancy was the accuracy of the turntable, which could be considered in line with the theoretical expectations.

4.3. Real-World Scenario Test Environment

Further comprehensive validation was conducted to assess the applicability of the model performance in real-world scenarios, aiming to deeply investigate the performance of the model under complex real-world conditions. We established an mmW frequency

band 5G-A commercial demonstration network test environment. It is important to note that the data used for analysis in this subsection came from large-scale field measurements. The sample size was sufficient, and the coverage was extensive, which effectively reflected the real-world situation. Based on this, this section provides a detailed introduction to the various comparative tests conducted on the low-altitude network sensing model based on ISAC base stations. Through multidimensional comparative analysis, we accurately evaluated the performance differences of the model under different conditions, providing solid data support for the optimization and practical application of the model.

The test area covered urban areas and towns, including residential buildings, small commercial streets, squares, etc. These areas are typical test scenarios. It was limited to the low-altitude area below 300 m and was a multi-cell networking scenario.

As shown in Figure 11, the test area covered 6 square kilometers and included 8 ISAC base stations with 19 sectors. The average inter-station distance was approximately 1 km. International equipment manufacturers provided the test base stations. The AAU had a vertical FOV of 40° and a mechanical tilt angle of 0°, with an average base station height of approximately 30 m. These parameters were incorporated into the single base station 3D sensing model, as shown in Figure 10. The sensing waveform combined a continuous wave and a pulse wave. The EIRP power of the continuous wave was 66 dBm, and the pulse wave was 75 dBm. The carrier configuration of the AAU is shown in Table 1. Except for the value of N ranging from 2 to 5 in the system, all the other parameters were the same as in Table 2.
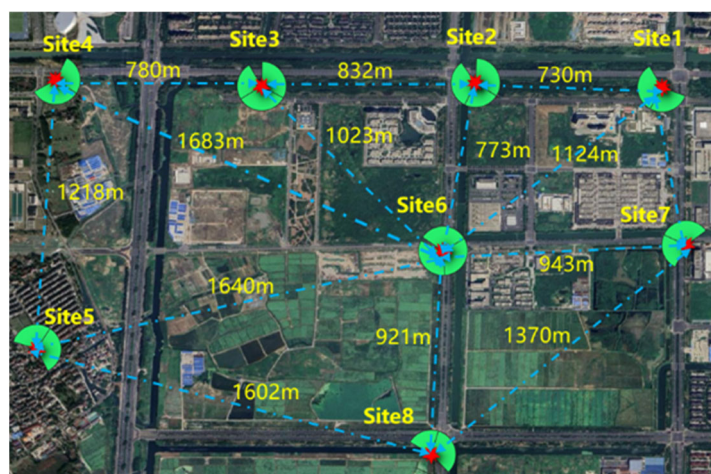

Figure 11. Single base station real-world scenario test environment.

The test UAV was a DJI Mavic 3, with unfolded dimensions of 347.5 mm × 283 mm × 107.7 mm (without propellers) and a diagonal wheelbase of 380.1 mm.

4.4. Single Base Station Sensing Validation

Single base station sensing tests were conducted in the real-world scenario test environment. Through multi-altitude, multi-directional flight tests, the effectiveness of the single base station 3D sensing model in real-world scenarios was verified, highlighting its advantages and shortcomings and providing a basis for model optimization and practical deployment.

We aimed to verify the practical ability of the single base station 3D sensing model to replicate sensing characteristics in real-world environments. To this end, a single base station sensing test was conducted with only the sector in one direction of Site 3 activated. The antenna of this station was at a height of 30 m, and the normal direction of the antenna is shown in Figure 12.

Figure 12. Single base station single direction test.

First, back-and-forth flight tests were conducted at heights of 30 m (base station height), 100 m, and 300 m, along both the antenna's normal direction and the direction with a horizontal deflection of 60°, as indicated by the red lines O_1P_1, O_1A_1, O_2P_2, O_2A_2, O_3P_3, and O_3A_3 in Figure 13. Subsequently, back-and-forth flight tests were performed along the horizontal normal direction (0°) with a vertical elevation angle of 40°, as shown by the blue line O_1C in Figure 13.
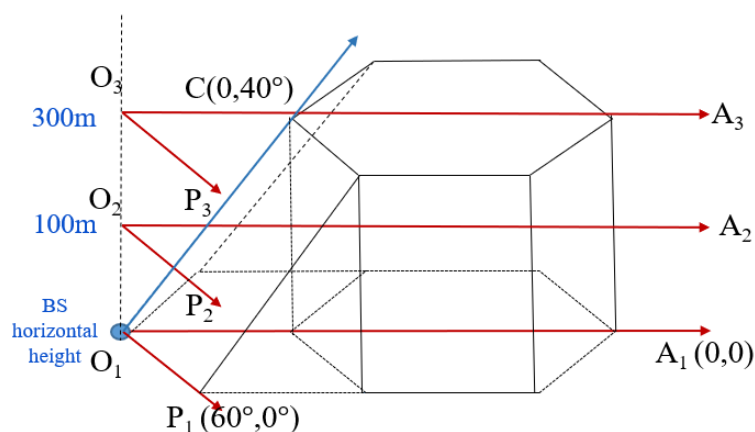

Figure 13. Single base station horizontal test routes.

Each direction was tested 100 times. The sensible radial and horizontal distances and the horizontal and vertical positioning accuracy within the sensing range were analyzed. The results are shown in Tables 5–7.

Table 5. Single base station horizontal direction test results.

Flight Path		Sensing Range								Sensing Accuracy at CDF 95%	
Flight Direction	Flight Height (m)	Nearest Radial Distance (m)	Nearest Horizontal Distance (m)	Farthest Radial Distance (m)	Farthest Horizontal Distance (m)	Nearest Theoretical Radial Distance (m)	Nearest Theoretical Horizontal Distance (m)	Farthest Theoretical Radial Distance (m)	Farthest Theoretical Horizontal Distance (m)	Horizontal Positioning Accuracy (m)	Vertical Positioning Accuracy (m)
Normal /O_1A_1	30	4.5	4.5	1051.4	1051.4	0.0	0.0	1000.0	1000.0	6.82	2.33
Normal/O_2A_2	100	100.8	75.4	1052.7	1050.4	108.9	83.4	1002.4	1000.0	6.86	2.88
Normal/O_3A_3	300	390.3	295.8	1068.7	1034.0	420.0	321.8	1035.8	1000.0	7.5	3.17
60°/O_1P_1	30	4.5	4.5	360.1	360.1	0.0	0.0	333.3	333.3	5.86	2.89
60°/O_2P_2	100		N/A				Out of the sensing range				N/A
60°/O_3P_3	300		N/A				Out of the sensing range				N/A

Table 6. Single base station horizontal direction error results.

Flight Path		Error Measurement of the Sensing Range				Sensing Accuracy at CDF 95%	
Flight Direction	Flight Height (m)	Nearest Radial Distance	Nearest Horizontal Distance	Farthest Radial Distance	Farthest Horizontal Distance	Horizontal Positioning Accuracy (m)	Vertical Positioning Accuracy (m)
Normal /O_1A_1	30	4.5m	4.5m	5.14%	5.14%	6.82	2.33
Normal/O_2A_2	100	7.44%	9.59%	5.02%	5.04%	6.86	2.88
Normal/O_3A_3	300	7.07%	8.08%	3.18%	3.4%	7.5	3.17
60°/O_1P_1	30	4.5m	4.5m	8.04%	8.04%	5.86	2.89

Table 7. Single base station upward tilt direction test results.

Flight Direction	Sensing Range						Sensing Accuracy at CDF 95%	
(0°, 40°)/O_1C	Measured farthest radial distance (m)	Theoretical radial distance (m)	Error percentage (%)	Measured nearest radial distance (m)	Theoretical nearest sensing radial distance (m)	Error value (m)	Horizontal positioning accuracy (m)	Vertical positioning accuracy (m)
	420.7	420.0	0.17	2.2	0	2.2	2.31	2.14

When analyzing the results in the horizontal direction, it is necessary to clarify the differences between the radial and horizontal directions. The radial direction refers to the straight-line direction from the antenna center to the target, where changes in the distance directly reflect the proximity of the target to the antenna. On the other hand, the horizontal direction focuses on the positional changes of the target in the horizontal cross-sectional plane relative to the antenna, emphasizing azimuthal information within the UAV.

In the flights at the base station height, the nearest sensing distance in the horizontal direction deviated from the theoretical expectation by 4.5 m. Analysis shows that this deviation was not caused by the model or measurement errors but rather by the limitations of the actual test conditions. During the UAV flight tests, safety considerations prevented the UAV from taking off immediately adjacent to the antenna, requiring a certain safety distance to be maintained. This prevented setting the test starting point at the theoretical 0 m position. In the horizontal direction, this safety distance resulted in a deviation between the actual starting point and the theoretical value. In the radial direction, it manifested as the flight starting radial distance being larger than the theoretical starting distance. Therefore, this deviation was caused by the difference between the actual test environment and the ideal conditions rather than by the model. The measured data within the constraints of the safety distance reasonably reflected the sensing capabilities of the single base station, which aligned with the expectations from the perspective of the actual test logic.

In the tests involving horizontal flight along the normal direction (3 OA paths), the farthest distances in both the radial and horizontal directions exceeded the theoretical values. The deviations ranged from 32.9 to 51.4 m across different heights, averaging 4.5% above the theoretical values. In the radial direction, the hardware design of the base station typically set the sensing range slightly larger than the theoretical value to mitigate coverage blind spots in complex environments, which increased the actual sensing farthest radial distance. Additionally, hardware limitations and factors such as beam fluctuations affected signal propagation, leading to deviations between the actual farthest radial distance and the theoretical value. In the horizontal direction, when the target was at the farthest distance, its positional deviation was also influenced by these factors. As the target radial distance changed, horizontal positioning changed.

For the nearest distances in horizontal flight along the normal direction, both the radial and horizontal distances were slightly smaller than the theoretical values, with deviations ranging from 8.0 to 29.7 m across different heights, averaging 8.0% below the theoretical

values. This was because hardware limitations and environmental interference prevented the signal from reaching the theoretical expectations at close distances during the actual tests. As a result, the actual nearest sensing radial distance was smaller than the theoretical value. In the horizontal direction, the reduction in radial distance affected the accuracy of the target positioning, leading to deviations from the theoretical values.

Similarly, in the tests involving flight in the horizontal direction (O_1P_1) at the base station height, the radial and horizontal distances deviated from the theoretical values by 26.8 m, with a deviation ratio of approximately 8%. The reasons were similar to the nearest distance deviations in the normal direction. During the actual measurements, the combined effects of safety distance, hardware performance, and environmental factors caused deviations between the measured and theoretical values in both the radial and horizontal directions. Notably, the UAV could not be sensed at higher heights along the OP paths, which was consistent with the theoretical expectations in both the radial and horizontal directions. From the radial perspective, the signal attenuated significantly with increasing distance, exceeding the sensing range. In the horizontal direction, the target exceeded the theoretical sensing horizontal range at that height, making it impossible to sense the UAV.

Based on these results, it can be concluded that the single base station sensing capabilities were consistent with the theoretical expectations. The single base station did have coverage blind spots, and the theoretical model accurately reflected the actual sensing range. The overall trend aligned well with the theoretical model.

On the other hand, within the sensing area, the horizontal and vertical positioning accuracies within the CDF 95% range were statistically analyzed. The horizontal accuracy ranged between 5.86 and 7.5 m. As the test height increased, the horizontal positioning accuracy slightly decreased, but it still met the specified requirements. According to Equation (2), the primary reason was that the UAV was not aligned with the antenna's normal direction, resulting in a decreased SNR and a reduced sensing accuracy. The overall accuracy in the OP direction was better than in the OA direction due to the difference in flight distance. OA paths generally cover longer distances, and according to Equation (1), the SNR degrades at farther points, resulting in relatively poorer accuracy in the OA direction during overall statistical analysis. The vertical accuracy fluctuated between 2.33 and 3.17 m, showing a trend consistent with the horizontal accuracy. The horizontal positioning accuracy was generally inferior to the vertical positioning accuracy due to the hardware design of the antenna array. The vertical direction had more antenna elements, and the larger element spacing caused by transmit–receive isolation resulted in a larger array aperture, providing a better angular accuracy and leading to superior vertical positioning accuracy. However, both the horizontal and vertical positioning accuracy values met the 3GPP TR 22.837 [29] requirement for UAV intrusion sensing, which specifies a positioning accuracy of less than 10 m, aligning with the expectations.

From the upward tilt direction test, it is clear that the measured farthest radial distance during upward flight was exceptionally close to the value of the theoretical model. An error of only 0.7 m represented an error ratio of approximately 0.17%. It shows that this minor deviation was primarily because of the impact of sensing accuracy. However, the deviation in the measured nearest sensing distance was relatively larger, reaching 2.2 m. The main reason for this was consistent with that in the horizontal direction. Namely, the starting point could not be set at 0 m in practical operations. It is worth noting that within the entire sensing range, when the positioning accuracy at CDF 95% was statistically analyzed, the results showed an accuracy of around 2 m, which fully met the sensing requirements.

To further verify the coverage blind spots caused by the vertical elevation angle and the ability of the single base station 3D sensing model to replicate the sensing range of

a real-world base station, targeted tests were conducted. According to Equation (10), the maximum horizontal distance of the blind spot was approximately 320 m. Vertical upward flights were performed at distances of 50 m, 100 m, 150 m, 200 m, 300 m, and 350 m along the antenna's normal direction (OA direction), as shown in Figure 14. To ensure data reliability, each point was tested 100 times. Subsequently, the minimum and maximum detectable heights at the corresponding positions and the horizontal and vertical positioning accuracies within the sensing range were analyzed in detail. The relevant results are summarized in Table 8.
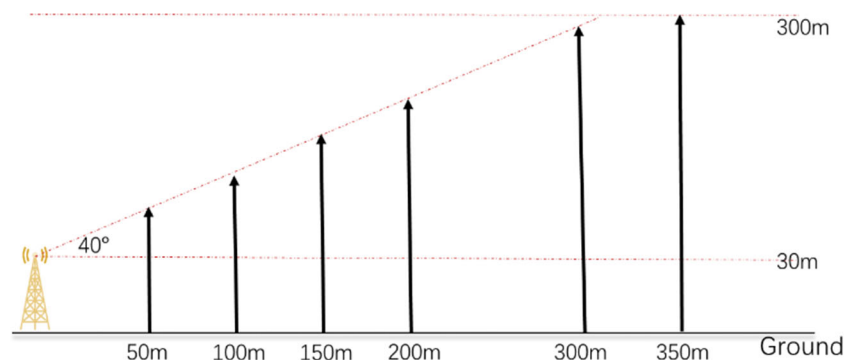
Figure 14. Single base station vertical test route.

Table 8. Single base station vertical direction test results.

Test Point (m)	Measured Minimum Height (m)	Theoretical Minimum Sensing Height (m)	Error Percentage (%)	Measured Maximum Height (m)	Theoretical Maximum Sensing Height (m)	Error Percentage (%)	Horizontal Positioning Accuracy at CDF 95% (m)	Vertical Positioning Accuracy at CDF 95% (m)
50	30.6		2	73.1	72.0	1.53	2.41	2.34
100	30.7		2.33	115.2	113.9	1.14	2.45	4.23
150	30.5	30	1.67	156.6	155.9	0.45	2.58	4.98
200	30.5		1.67	199.9	197.8	1.06	3.26	3.93
300	31.1		3.67	281.8	281.7	0.04	3.11	2.94
350	30.6		2	301.0	300	0.33	3.34	3.74

In terms of the minimum sensing height, the sensing range was between 30.5 and 31.1 m, with an average of approximately 30.6 m, which was about 2% higher than the actual height of the base station. Considering the slight deviation between the actual mechanical installation angle of the base station and the theoretical normal direction, as well as the impact of positioning accuracy errors, it can be concluded that the results aligned with the theoretical model expectations. This validates the lower coverage limit of the base station antenna in the vertical direction.

Regarding the maximum sensing height, the measured results were consistent with the theoretical value, with a maximum error of 2.1 m and an overall error range of 0–1.53%. The highest sensing heights during vertical flights at all test points were slightly greater than the corresponding theoretical vertical sensing boundary heights. This discrepancy was related to the antenna installation angle errors and sensing accuracy limitations. It can be concluded that the results were generally consistent with the theoretical expectations, verifying the coverage blind spots caused by the vertical FOV. This demonstrates that the theoretical model accurately predicted the maximum sensing height.

The horizontal and vertical positioning accuracies within the CDF 95% range were statistically analyzed within the sensing range. The horizontal accuracy varied slightly across different test points, ranging between 2.41 m and 3.34 m. The horizontal positioning accuracy slightly decreased as the distance increased, but it still met the specified requirements. The primary reason, as indicated by Equation (1), was that the increase in distance led to a decrease in the SNR, further reducing sensing accuracy. The vertical accuracy

fluctuated between 2.34 and 4.98 m, showing no strong correlation with distance. The poorest performance occurred at the 150 m horizontal distance point, primarily because the flight trajectory near the base station height formed a small angle with the radial vertical tangent of the AAU, resulting in an unstable sensing performance. However, both the horizontal and vertical positioning accuracies were significantly below the upper limit of the specified requirements, aligning with the expectations.

By comprehensively traversing the sensing range in multiple directions, the measured results and the theoretical analysis exhibited the same trend. Thus, the theoretical model proposed in Section 2.3 effectively replicated the real-world sensing capabilities with an accuracy rate exceeding 92%.

4.5. Networked Sensing Validation

The single base station sensing tests evaluated the performance of individual stations, while the multi-BS networked sensing test delved into the model performance from a wide-area sensing perspective. These tests involved constructing base stations based on a multi-BS cellular-like topology and adjusting relevant parameters to assess the key metrics of the model under networked conditions, focusing on verifying the improvement in single base station sensing blind spots. This provides support for the planning and construction of base station networks.

When validating the performance of the multi-BS cellular-like topology sensing model, the first step is to select and construct the ISAC base stations according to the theoretical multi-BS cellular-like topology. This topology achieves continuous sensing at different heights by spatially stretching and translating the traditional cellular communication topology in the vertical dimension, enabling cellular-like networked sensing across horizontal cross-sections at various altitudes. From Section 3, the station spacing d and the coverage radius R must satisfy $d \leq R$ to ensure seamless coverage. On this basis, the sector's normal directions and vertical elevation angles of each station were finely adjusted to align as closely as possible with the theoretical model, ensuring the accuracy of the tests. After completing the base station deployment, the sensing functions of all sectors in the ISAC base stations were activated, constructing a comprehensive multi-BS sensing network.

Systematic sensing tests were conducted within the test area under the networked configuration. The UAV was selected as the test target, and tests were performed at 100 m and 300 m above the ground. The UAV flew at a stable speed of 5 m/s along a planned route, which is precisely designed to ensure that the UAV sequentially passed through the coverage areas of each station, thereby comprehensively detecting the sensing performance of the base stations at different locations. To ensure the reliability and representativeness of the test data, each flight height involved repeated traversals of the entire coverage area, with no fewer than 1200 valid sample points collected for each flight height.

From the test results (as shown in Figures 15–18), in areas near the Site 1/2/6/7 base stations at various heights, the sensing SNR and accuracy performed well due to the station locations being more aligned with the multi-BS cellular-like topology model. However, in some areas, abnormal sensing accuracy was observed. For example, occasional scattered points with accuracy below the specified threshold were primarily caused by the overlap of the flight route with roads, where reflections from large ground vehicles introduced clutter interference. This interference reduced the sensing SNR, thereby affecting sensing accuracy.

Figure 15. Multi-BS sensing test results at the altitude of 100 m–SNR.

Figure 16. Multi-BS sensing test results at the altitude of 100 m–positioning accuracy.

Figure 17. Multi-BS sensing test results at the altitude of 300 m–SNR.
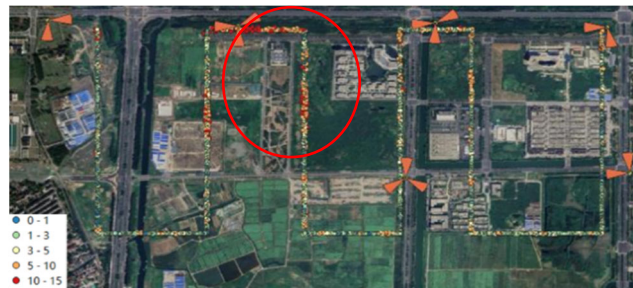

Figure 18. Multi-BS sensing test results at the altitude of 300 m–positioning accuracy.

Specifically, in the red-circled area near Site 3, the actual construction location of Site 5 significantly deviated from the theoretical model, resulting in the blind spot of Site 3 not being effectively covered by Site 5. This led to a lower sensing SNR in this area, directly causing degraded sensing performance. Moreover, as the height increased, such as at 300 m, the blind spot area became larger than that at 100 m, resulting in an

increased number of points with poor performance. This phenomenon aligned with the theoretical expectations.

Further analysis revealed that the distribution trends of accuracy and the SNR were similar. In areas with a lower SNR, the accuracy values are also poorer. The CDF curves are obtained by statistically analyzing the SNR and positioning accuracy across the entire test route, as shown in Figure 19. Taking the CDF 95% statistical value, the overall horizontal and vertical positioning accuracies along the flight route were determined, as shown in Table 9. The previously derived equation showed that the theoretical minimum sensing SNR was 13 dB. The statistical results showed that, regardless of the flight height, over 99.9% of the points along the entire flight route met this requirement. Therefore, it can be concluded that no sensing blind spots existed within the test area.
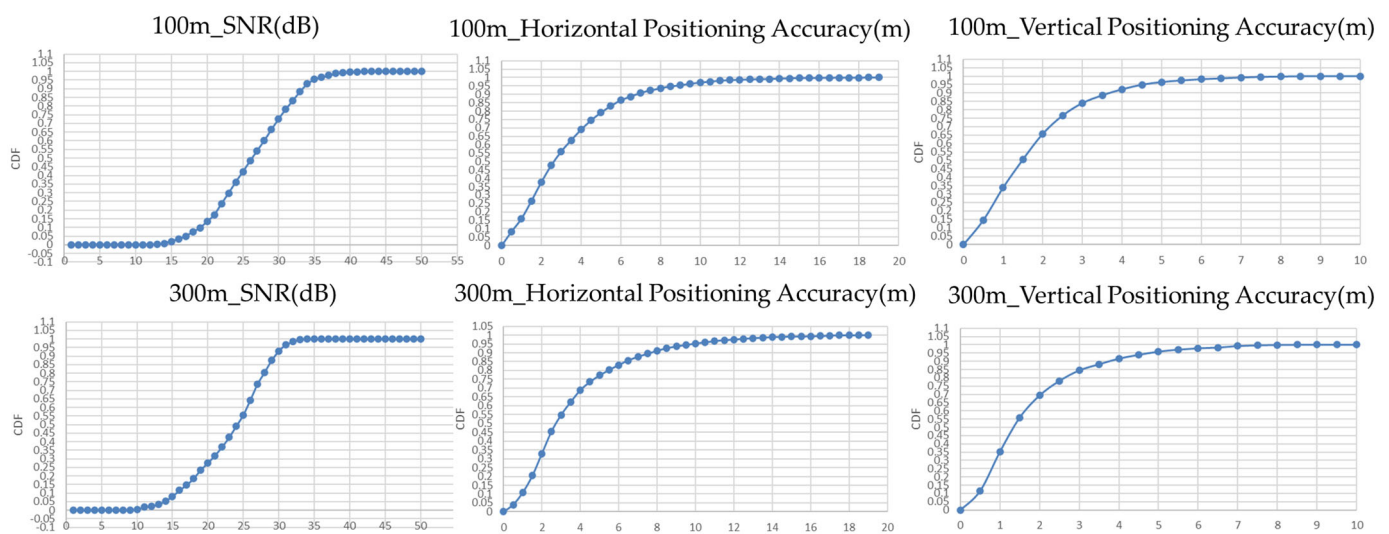
Figure 19. Multi-BS sensing test CDF.

Table 9. Multi-BS sensing test result.

Height (m)	Horizontal Positioning Accuracy at CDF 95% (m)	Vertical Positioning Accuracy at CDF 95% (m)
100 m	8.49	4.51
300 m	8.72	4.78

Compared to the single base station test results, the overall average horizontal and vertical positioning accuracies in the networked environment were relatively worse. This was primarily due to the increased complexity of the networked environment, where operations such as trajectory fusion and target deduplication among multiple stations introduced additional sources of errors. However, the overall positioning accuracy still met the sensing performance requirement of less than 10 m, and the vertical accuracy was generally better than the horizontal accuracy, which aligned with the theoretical expectations.

In summary, the multi-BS cellular-like topology sensing model demonstrated significant advantages in practical tests. It effectively addressed the issue of single base station sensing blind spots and accurately replicated the actual sensing capabilities in real-world scenarios. This provides reliable theoretical references and practical insights for the future planning and construction of ISAC base stations.

5. Conclusions

This paper investigated a low-altitude sensing model based on ISAC. First, we discussed the 3D sensing capabilities of a single base station. Subsequently, considering the differences between low-altitude sensing and traditional communication networks, we designed a single base station 3D sensing model. Furthermore, we proposed a multi-BS cellular-like topology to achieve a continuous and seamless low-altitude sensing network. Finally, we conducted actual tests that validated the practical performance. In this paper, all results were based on the first commercial ISAC network. We utilized mainstream equipment vendors to build the test environment and analyze the collected data. The single base station sensing model was verified to effectively replicate the sensing range of a single ISAC base station. Meanwhile, the multi-BS topology effectively mitigated sensing blind spot issues. The research innovatively proposed a mathematical model for qualitatively evaluating the sensing range, which exhibits universality and applicability. It can be extended to various networked sensing designs. This is crucial for the future development of wide-area 3D sensing networks.

Abbreviations

The following abbreviations are used in this manuscript:

2D	Two-dimensional
3D	Three-dimensional
AAU	Active antenna unit
BBU	Baseband unit
CoMP-JT	Coordinated multi-point joint transmission
FOV	Field of view
ISAC	Integrated sensing and communication
LOS	Line-of-sight
mmW	Millimeter wave
multi-BS	Multi-base station
NLOS	Non-line-of-sight
OTA	Over-the-air
RCS	Radar cross-section
RSRP	Reference signal receiving power
SCA	Successive convex approximation
SNR	Signal-to-noise ratio
UAV	Unmanned aerial vehicle

References

1. Nwaogu, J.M.; Yang, Y.; Chan, A.P.; Chi, H.L. Application of drones in the architecture, engineering, and construction (AEC) industry. *Autom. Constr.* **2023**, *150*, 104827. [CrossRef]

2. Mei, X.; Miao, F.; Wang, W.; Wu, H.; Han, B.; Wu, Z.; Chen, X.; Xian, J.; Zhang, Y.; Zang, Y. Enhanced Target Localization in the Internet of Underwater Things through Quantum-Behaved Metaheuristic Optimization with Multi-Strategy Integration. *J. Mar. Sci. Eng.* **2024**, *12*, 1024. [CrossRef]

3. Miao, F.; Li, H.; Yan, G.; Mei, X.; Wu, Z.; Zhao, W.; Liu, T.; Zhang, H. Optimizing UAV Path Planning in Maritime Emergency Transportation: A Novel Multi-Strategy White Shark Optimizer. *J. Mar. Sci. Eng.* **2024**, *12*, 1207. [CrossRef]

4. Markets and Markets. *Smart Cities Market Analysis, Industry Size and Forecast, High Tech, Enterprise & Consumer IT*; Markets and Markets: Pune, India, 2022.

5. China Telecom Corporation Limited. White Paper on Integrated Air-Ground 5G-Enhanced Low-Altitude Network. In Proceedings of the Global System for Mobile Communications Association (GSMA) Mobile World Congress (MWC), Barcelona, Spain, 24–29 February 2024.

6. Li, R.; Xiao, Z.; Zeng, Y. Toward Seamless Sensing Coverage for Cellular Multi-Static Integrated Sensing and Communication. *IEEE Trans. Wirel. Commun.* **2024**, *23*, 5363–5376.

7. Zuo, M.; Wu, Y.H.; Cheng, J. Research on Coverage Schemes and Deployment Strategies for Low-Altitude 5G Networks. *Electron. Technol. Softw. Eng.* **2022**, *20*, 32–35.

8. Fan, C.X. *Principles of Communications*, 7th ed.; National Defense Industry Press: Beijing, China, 2013; p. 45.

9. China Mobile Fujian Co., Ltd.; China Mobile Communications Group Co., Ltd.; Chengdu Industrial Research Institute Branch; HuaWei Technologies Co., Ltd. White Paper on 3D Coverage Network for Drones Based on 5G Communication Technology. In Proceedings of the Global System for Mobile Communications Association (GSMA) Mobile World Congress (MWC), Barcelona, Spain, 28 February–3 March 2022.

10. Zhen, Z.G.; Ji, G.Q. Research on Private Networks for 5G Low-Altitude Coverage. In Proceedings of the 2018 5G Network Innovation Seminar, Beijing, China, 23 August 2018.

11. IMT-2020 (5G) Promotion Group. *5G-Advanced Integrated Sensing and Communication Air Interface Technology Solution Research Report*, 2nd ed.; IMT-2020 (5G) Promotion Group: Beijing, China, 2024.

12. Qu, S.H.; Xu, L.F.; Cheng, S.W. Research on the Detection Performance of Low-Altitude UAVs Using 5G-A Integrated Communication and Sensing Technology. *Telecom Eng. Tech. Stand.* **2024**, *37*, 75–80.

13. Li, R.; Xiao, Z.; Zeng, Y. Beamforming towards seamless sensing coverage for cellular integrated sensing and communication. In Proceedings of the 2022 IEEE International Conference on Communications Workshops (ICC Workshops), Seoul, Republic of Korea, 16–20 May 2022.

14. Lei, Z.; Chen, X.; Tan, Y. A Coverage Model of FMCW Radar for Optimizing Sensor Network Deployment. *IEEE/ASME Trans. Mechatron.* **2024**, *29*, 2991–3000. [CrossRef]

15. Wang, B.; Wang, Y.; Li, N.; Zhu, J.; She, X.; Chen, P. On Collaborative Sensing of Cellular Networks Under Mutual Signal Interference. *IEEE Wirel. Commun. Lett.* **2024**, *13*, 2531–2535. [CrossRef]

16. Zhao, L.B.; Luo, H.L.; Gao, F.F. Integrated Sensing, Communication, and Computing for Low-Altitude UAV Networks: A Base Station-Centric Approach. *Mob. Commun.* **2024**, *48*, 57–63+70.

17. Wang, X.; Han, Z.; Jin, J.; Xi, R.; Wang, Y.; Han, L.; Ma, L.; Lou, M.; Gui, X.; Wang, Q.; et al. Multistatic Integrated Sensing and Communication System Based on Macro–Micro Cooperation. *Sensors* **2024**, *24*, 2498. [CrossRef] [PubMed]

18. Azari, M.M.; Rosas, F.; Chiumento, A.; Pollin, S. Coexistence of Terrestrial and Aerial Users in Cellular Networks. In Proceedings of the 2017 IEEE Globecom Workshops (GC Wkshps), Singapore, 4–8 December 2017.

19. Goddemeier, N.; Daniel, K.; Wietfeld, C. Coverage evaluation of wireless networks for Unmanned Aerial Systems. In Proceedings of the 2010 IEEE Globecom Workshops, Miami, FL, USA, 6–10 December 2010.

20. Lyu, J.; Zhang, R. Network-Connected UAV: 3-D System Modeling and Coverage Performance Analysis. *IEEE Internet Things J.* **2019**, *6*, 7048–7060. [CrossRef]

21. Elnoubi, S.M. Three-dimensional cellular systems for air/ground personal communication. *IEEE Trans. Veh. Technol.* **2005**, *54*, 1923–1931. [CrossRef]

22. Cho, H.; Chung, J.H.; Sung, D.K. Four-sector cross-shaped urban microcellular systems with intelligent switched-beam antennas. *IEEE Trans. Veh. Technol.* **2001**, *50*, 592–604.

23. Wang, L.C.; Leung, K.K. A high-capacity wireless network by quad-sector cell and interleaved channel assignment. *IEEE J. Sel. Areas Commun.* **2000**, *18*, 472–480.

24. Chen, S. Discussion on Establishing Wireless Three-dimensional Communication Network in Low Altitude Airspace. *Commun. Technol.* **2022**, *55*, 1456–1463.

25. Zhao, J.X.; Ruan, X.B. Discussion on Low-Altitude Coverage Networking for UAV IoT Based on 5G Communication. *Guangxi Commun. Technol.* **2022**, *4*, 1–8.

26.	Fan, M.B.; Zhang, Y.; Li, R.F. Research on 5G-A Integrated Sensing and Communication Networking Strategies for Low-Altitude Applications. *Commun. World* **2024**, *17*, 32–36.

27.	Ding, L.F.; Geng, F.L.; Chen, J.C. *Principles of Radar*, 6th ed.; Publishing House of Electronics Industry: Beijing, China, 2020; p. 174.

28.	3GPP. "Study on Channel Model for Frequencies from 0.5 to 100 GHz", 3rd Generation Partnership Project (3GPP), Technical Report (TR) 38.901, 03 04 2022, Version 18.0.0. Available online: https://portal.3gpp.org/desktopmodules/Specifications/SpecificationDetails.aspx?specificationId=3173 (accessed on 6 February 2025).

29.	3GPP. "Study on Integrated Sensing and Communication", 3rd Generation Partnership Project (3GPP), Technical Report (TR) 22.837, 28 06 2024, Version 19.4.0. Available online: https://portal.3gpp.org/desktopmodules/Specifications/SpecificationDetails.aspx?specificationId=4044 (accessed on 6 February 2025).